# Observed equatorward propagation and chimney effect of near-inertial waves in the mid-latitude ocean

**Xiaolong Yu[1,2,3], Alberto C. Naveira Garabato[4], Clément Vic[5], Jonathan Gula[5,6], Anna C. Savage[7], Jinbo Wang[8], Amy F. Waterhouse[7], Jennifer A. MacKinnon[7]**

[1]School of Marine Sciences, Sun Yat-sen University, Zhuhai, China
[2]Southern Marine Science and Engineering Guangdong Laboratory (Zhuhai), Zhuhai, China
[3]Guangdong Provincial Key Laboratory of Marine Resources and Coastal Engineering, Guangzhou, China
[4]Ocean and Earth Science, University of Southampton, Southampton, UK
[5]Univ Brest, CNRS, IRD, Ifremer, Laboratoire d'Océanographie Physique et Spatiale (LOPS), IUEM, Brest, France
[6]Institut Universitaire de France (IUF), Paris, France
[7]Scripps Institution of Oceanography, University of California, San Diego, La Jolla, California, USA
[8]Jet Propulsion Laboratory, California Institute of Technology, Pasadena, California, USA

**Key Points:**

- We provide observational evidence of downward- and equatorward-propagating near-inertial waves over a full annual cycle.
- Enhanced near-inertial kinetic energy and vertical shear are found preferentially in regions of anticyclonic vorticity.
- The chimney effect for near-inertial waves is controlled by mesoscale, rather than submesoscale, anticyclones.

Corresponding author: Xiaolong Yu, yuxlong5@mail.sysu.edu.cn

## Abstract

The propagation characteristics of near-inertial waves (NIWs) and how mesoscale and submesoscale processes affect the waves' vertical penetration (i.e., the chimney effect) are investigated using observations from a mooring array located in the northeast Atlantic. The year-long observations show that near-inertial motions are mainly generated by local wind forcing and that they radiate predominantly downward following several strong wind events (wind stress$\gtrsim$0.5 N m$^{-2}$). Once below the mixed layer, NIWs preferentially propagate equatorward primarily in the form of low modes. High-mode NIWs, however, are most likely dissipated locally near the base of the mixed layer. Enhanced near-inertial kinetic energy and vertical shear are found only in mesoscale anticyclones with Rossby number of O(0.1). By contrast, submesoscale motions with order one Rossby number have little effect on the trapping and vertical penetration of NIWs, due to their smaller horizontal scales and confined vertical extent compared to mesoscale eddies.

## Plain Language Summary

Near-inertial waves (NIWs) are excited mainly by variable winds at the ocean surface and can carry their energy into the ocean interior, thus playing an important role in mixing the deep ocean. However, the propagation behaviors of NIWs, and how such waves are affected by mesoscale and submesoscale processes, are still understudied, especially over periods of months to years. In this study, we examine an annual cycle of wind-generated NIWs based on moored observations in a typical open-ocean region of the northeast Atlantic. Our results show that NIWs predominately propagate downward and equatorward following several strong wind events. Enhanced near-inertial kinetic energy and vertical shear are found preferentially in regions of anticyclonic vorticity with Rossby number of O(0.1). By contrast, submesoscale anticyclones with Rossby number of O(1) are ineffective at trapping and accelerating near-inertial motions into the ocean interior. This is due to the smaller horizontal scales and confined vertical extent of submesoscale motions compared to mesoscale eddies. Our findings highlight the major role of mesoscale anticyclones in draining NIWs from the upper ocean to the ocean interior, and have implications for detecting regions of active turbulent mixing driven by NIWs in the deep ocean.

# 1 Introduction

Near-inertial waves (NIWs), primarily generated by strong resonant winds blowing on the sea surface, are a crucial contributor to ocean mixing (Alford et al., 2016; Thomas & Zhai, 2022). NIWs are oscillatory, unbalanced motions with frequencies close to the local inertial frequency, and account for a major portion of internal wave energy and shear (Garrett, 2001). Wind generation of near-inertial motions can be generally considered as a two-stage process, featuring an initial stage with wind resonance that generates surface mixed-layer near-inertial oscillations, and a subsequent stage with propagation and decay of those motions in the form of NIWs. Global estimates of the wind energy flux into NIWs are in the range of 0.3-1.5 TW (Jiang et al., 2005; Rimac et al., 2013), which is comparable to the global energy conversion rate from external to internal tides in the deep ocean (about 1 TW; Egbert & Ray, 2000). Although over half of near-inertial energy is thought to dissipate in the upper few hundred meters of the ocean (Zhai et al., 2009; Alford, 2020), the rest of the wave energy has been suggested to predominately radiate downward (e.g., Leaman & Sanford, 1975; Gill, 1984) and to penetrate to large depths (e.g., 3000 m; Silverthorne & Toole, 2009). Hence, the substantial downward-propagating NIWs are an important source of energy for driving deep-ocean mixing and maintaining abyssal stratification (Ferrari & Wunsch, 2009; Whalen et al., 2020; Qu et al., 2021).

A key factor that affects the vertical penetration of NIWs is the background vorticity. The principal effect of vorticity is to shift the lower bound of the internal wave band, and consequently NIWs can be trapped in regions of negative relative vorticity where the effective inertial frequency is reduced (Kunze, 1985). Lee and Niiler (1998) firstly termed this phenomenon as the inertial chimney effect, which allows near-inertial energy accumulation and rapid deep propagation. The inertial chimney effect has been explored by, for example, Zhai et al. (2005, 2007), who analyzed mesoscale-permitting numerical simulations to show that anticyclonic eddies act to drain near-inertial energy from the surface to the deep ocean. More recently, the inertial chimney effect of turbulent baroclinic quasi-geostrophic eddies was also demonstrated by Asselin and Young (2020) under an idealized storm scenario, where they referred to this effect as 'inertial drainpipe'. Vic et al. (2021) examined the association of mooring-measured near-inertial energy with altimetry-derived relative vorticity with a horizontal resolution of O(100 km) over the Mid-Atlantic Ridge, and showed that near-inertial energy is preferentially funneled down within anticyclonic flows. To our knowledge, observational assessment of the chimney effect down to the submesoscales (0.1-10 km) has not yet been performed.

Compared to the dominant downward propagation of NIWs, their meridional propagation, however, remains elusive. The theory of $\beta$-refraction predicts an equatorward propagation of NIWs due to the latitudinal variation in the inertial frequency (Garrett, 2001). This proposition is endorsed by near-inertial energy flux estimates from mooring observations in the open ocean (e.g., Alford, 2003) and on the continental shelf (e.g., Schlosser et al., 2019). Such calculations typically require a flat-bottomed ocean and full-depth measurements, and thus existing observations are sparse. By contrast, numerical and observational studies have also shown that NIWs can propagate poleward. Based on turning-point theory and a numerical model, Fu (1981) suggested that the observed local inertial peak over smooth topography could be interpreted in terms of poleward-propagating waves generated at lower latitudes. The poleward propagation of NIWs can also be caused by the background flow (e.g., Tort & Winters, 2018; Jeon et al., 2019; Huang et al., 2021). Tort and Winters (2018) demonstrated a scale selection mechanism by which the super-inertial component of NIWs is able to propagate poleward over long distances in the presence of mesoscale turbulence with horizontal scales considerably smaller than the width of the storm track.

In this study, we focus on the propagation of NIWs in a typical mid-ocean region using nine year-long mooring records that resolve the spatio-temporal scales of the submesoscales. We show that wind-generated NIWs predominately propagate downward and equatorward in the study region. The waves' vertical and meridional group speeds are directly quantified from observations, and are found to be consistent with the properties determined by the dispersion relation. The inertial chimney effect is observed below the mixed layer. However, enhanced near-inertial kinetic energy and vertical shear are only found in mesoscale anticyclones of Rossby number O(0.1) rather than in submesoscale anticyclones of Rossby number O(1).

# 2 Observations and Methods

## 2.1 Mooring observations

Nine bottom-anchored subsurface moorings were deployed over the Porcupine Abyssal Plain (48.63-48.75°N, 16.09-16.27°W) site in the northeast Atlantic Ocean for the period September 2012 - September 2013 (Figure 1a), as part of the OSMOSIS (Ocean Surface Mixing, Ocean Submesoscale Interaction Study) experiment (Buckingham et al., 2016, 2019; Yu et al., 2019, 2021; Naveira Garabato et al., 2022). The mooring site is over a smooth abyssal plain of depth close to 4800 m. This region is expected to be representative of the mid-latitude open ocean far away from western boundaries and complex topography. The nine moorings were arranged in two concentric quadrilaterals with side lengths of $\sim$13 km (outer cluster) and $\sim$2 km (inner cluster) around a centrally located single mooring (Figure 1b). Mooring sensors comprised a series of paired Nortek Aquadopp acoustic current meters (ACMs) and Seabird MicroCAT conductivity-temperature-depth (CTD) sensors at different depths, spanning the approximate depth interval 30-530 m. The central mooring was the most heavily instrumented, with 13 CTD/ACM pairs. The inner and outer moorings had seven and five such pairs, respectively. The central and four inner moorings were also instrumented with 75-KHz unit upward-looking Acoustic Doppler Current Profilers (ADCP) at about 450 m, which measured horizontal velocity in 8-m bins and formed ensembles every 60 minutes. In addition, the mooring measurements were complemented by hydrographic observations acquired by two ocean gliders that navigated in a bow-tie pattern across the mooring array for the entire sampling period (Damerell et al., 2016; Thompson et al., 2016). The mixed layer depth, $H_{ML}$, is calculated from coincident glider data using a threshold value of potential density increase ($\triangle\rho = 0.03$ kg m$^{-3}$) from a near-surface value at 10 m (Damerell et al., 2016).

Mooring measurements captured the mixed layer during winter and early spring months, and the pycnocline plus part of the ocean interior throughout the year. Horizontal velocity, temperature, salinity and pressure observations were obtained by ACMs and CTDs, with sampling intervals of 10 and 5 minutes, respectively. For each mooring, we linearly interpolated measurements of horizontal velocity, temperature and salinity onto surfaces of constant depth at 10-m intervals between depths of 50 m and 520 m, and onto uniform 10-minute intervals between 5 September 2012 and 5 September 2013. Subsequently, the 10-minute horizontal velocities were averaged onto hourly intervals.

## 2.2 Wind data

The buoy of the OSMOSIS moorings contained meteorological sensors. Unfortunately, the buoy sank shortly after deployment. Wind data are instead taken from the ECMWF (European Centre for Medium-Range Weather Forecasting) ERA-Interim reanalysis surface wind fields (Dee et al., 2011). Zonal and meridional reanalysis winds are obtained at the grid point closest to the central mooring site with a time interval of 3 hours for the record year. Wind measurements from the K1 buoy, 250 km away from the OSMOSIS mooring site (Figure 1a), are used to validate the reanalysis wind fields. The K1 buoy sampled at hourly intervals from 5 September to 28 December 2012. Wind speed was converted to stress using a speed-dependent drag coefficient (Large & Pond, 1981). The reanalysis winds show a good agreement with the measured winds, with a correlation coefficient of 0.74 (Figure 1c).

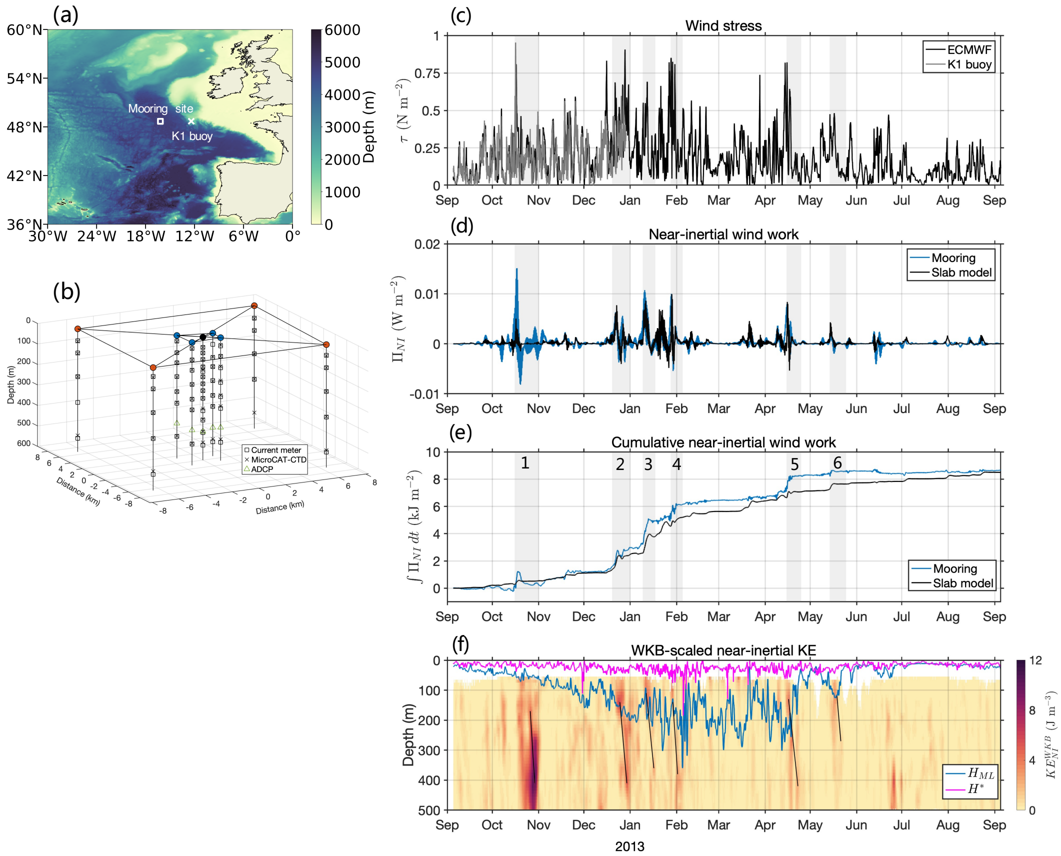


**Figure 1.** (a) OSMOSIS study region in the Northeast Atlantic, with bathymetry shown in the colormap on the right. The white rectangle and white cross denote the locations of the OSMOSIS mooring array and the K1 buoy, respectively. (b) 3-d configuration of the OSMOSIS array (central mooring marked by black circle, inner moorings by blue circles, and outer moorings by red circles), with positions of current meters, CTDs and ADCPs respectively marked by black squares, black crosses and green triangles. (c) Time series of wind stress estimated from the ECMWF reanalysis winds (black) and the K1 buoy measurements (gray). (d) Time series of near-inertial wind work computed from the ECMWF reanalysis winds and observed mixed-layer near-inertial currents (blue), and from the slab model driven by the ECMWF reanalysis winds (black). (e) Time integral of (d) showing the cumulative wind energy input to the mixed layer from each flux estimate for the central mooring deployment period. (f) Time series of WKB-scaled near-inertial kinetic energy observed by the current meters at the central mooring. The black and pink lines respectively indicate the glider-based mixed layer depth $H_{ML}$ and the $H^*$ scaling (section 3.1). Periods of the six near-inertial events are shaded gray in (c-e) and are labeled in (e). The duration of each event is mainly chosen to include near-inertial energy peaks from all moorings. The implied downward group velocity of each event is indicated in (f).

### 2.3 Band pass filtering

Moored horizontal velocities are bandpass filtered around the near-inertial frequency, where the near-inertial band (denoted by the subscript '$NI$') is defined as $\{0.9,\ 1.1\}f$, with $f = 2\Omega \sin\phi$ as the inertial frequency, $\Omega$ as the Earth's angular velocity and $\phi$ as latitude. The inertial period is approximately 16 hr at the OSMOSIS site. The rotary frequency spectra of horizontal velocity show a prominent peak rising within the near-inertial band for clockwise motions but not for counter-clockwise motions, consistent with the expectation that near-inertial flows are strongly clockwise-polarized (Figure S1 in the supporting information). We did not find a significant sensitivity of our results (section 3) to the bandwidth of the near-inertial band. Near-inertial velocity is isolated by means of a fourth-order Butterworth filter applied in the time domain. Following bandpassing, near-inertial kinetic energy and vertical shear are respectively quantified as $KE_{NI} = \frac{1}{2}\rho_0|\boldsymbol{u}_{NI}|^2$ and $S_{NI} = |\partial\boldsymbol{u}_{NI}/\partial z|^2$, where $\boldsymbol{u} = (u, v)$ is the horizontal velocity, $\rho_0 = 1025$ kg m$^{-3}$ is a reference density and $z$ is the vertical coordinate. As previous OSMOSIS studies have shown that the region underwent a seasonal cycle in the vertical stratification (e.g., Buckingham et al., 2016; Erickson et al., 2020), monthly moving averaged buoyancy frequency is used to obtain 'Wentzel-Kramers-Brillouin (WKB)' scaled near-inertial kinetic energy $KE_{NI}^{WKB}$ and vertical shear $S_{NI}^{WKB}$ (see the supporting information for methodology). Further, the near-inertial wind work is defined as $\Pi_{NI} = \boldsymbol{\tau}_{NI} \cdot \boldsymbol{u}_{NI}$, where $\boldsymbol{\tau}$ is the surface wind stress vector and $\boldsymbol{u}_{NI}$ the mixed-layer near-inertial currents obtained from the shallowest available ACMs record in the central mooring ($\sim$50 m, 57.1% of the time during the year within the mixed layer).

## 3 Results

### 3.1 Annual cycle of wind-generated near-inertial waves

Near-inertial wind work is highly variable throughout the entire year, with the wind energy flux into near-inertial motions dominated by several intermittent events with duration of several days (Figure 1d). The cumulative near-inertial wind work with time shows a distinct 'staircase' structure during the periods of strong resonant forcing (Figure 1e), which coincides well with the elevated $KE_{NI}^{WKB}$ in the upper ocean (e.g., late December and mid-January; Figure 1f). These results suggest that the observed near-inertial energy is likely locally generated by surface wind forcing. This is further supported by the agreement between the near-inertial wind work estimated from observed velocity and reanalysis winds and that from the slab model solely forced by the reanalysis winds (see the supporting information for methodology). The typical amplitude of $KE_{NI}^{WKB}$ during near-inertial wave events is of order 10 J m$^{-3}$, corresponding to a horizontal velocity scale of $\sim$0.1 m s$^{-1}$. This value is comparable in magnitude with the global average near-inertial velocity (Park et al., 2005; Chaigneau et al., 2008). Further, most of the increase in cumulative near-inertial wind work is seen in winter (December-March; Figure 1e), implying a seasonal cycle of wind-generated NIWs. Indeed, the seasonality is more apparent in the vertical profiles of $KE_{NI}^{WKB}$ in winter and summer (Figure S2), with the magnitude being much higher in winter at all measured depths.

Alford (2020) indicated that the slab model might overestimate the near-inertial wind work when the mixed layer depth $H_{ML}$ is shallow compared to the scaling $H^* = u^*/\sqrt{N^* f}$, where $u^* = \sqrt{\tau/\rho_{air}}$ is the friction velocity of the imposed stress, $\rho_{air}$ the density of air and $N^*$ the buoyancy frequency just below the mixed layer. In the $H_{ML} \lesssim H^*$ case, the slab model may not account for the mixing and momentum injected by the winds. We examined this possibility in our data and found that the glider-derived mixed layer depth is largely deeper than $H^*$ throughout the year, with the only exception in summer when $KE_{NI}^{WKB}$ is weak (June-August).

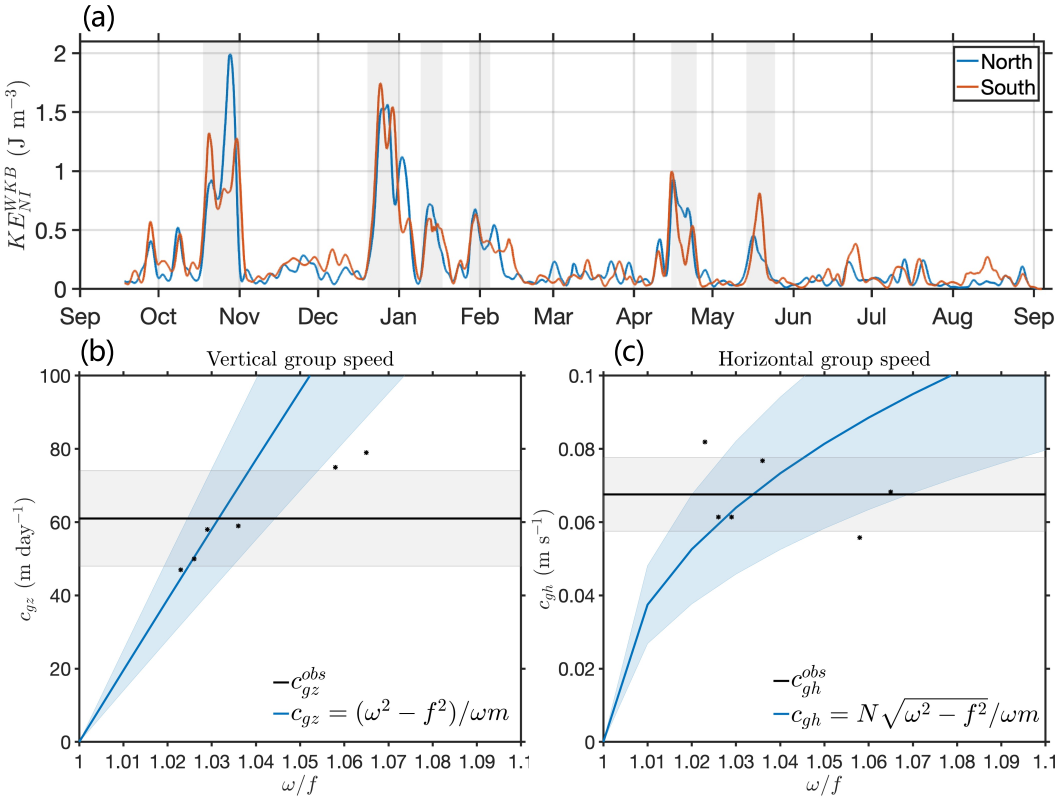


**Figure 2.** (a) Time series of WKB-scaled near-inertial kinetic energy estimated from outer moorings in the north (blue) and south (orange). Both estimates are low-pass filtered over 14.5 hr (corresponding to a frequency of $1.1f$) to remove tidal and higher-frequency signals, and are then depth-averaged over all observed depths (50-520 m). (b) Comparison of six event-averaged vertical group speed estimates from observations (black) and from the dispersion curve for $m = 2\pi/652$ m (blue). The shading represents one standard deviation. (c) Same as (b) but for horizontal group speed. Scattered dots in (b-c) represent estimates of the six near-inertial wave events.

### 3.2 Downward and equatorward propagation of near-inertial waves

Six major near-inertial wave events are identified throughout the year (see Figure 1e), based on large wind stress ($\gtrsim$0.5 N m$^{-2}$), net near-inertial wind energy input and enhanced near-inertial kinetic energy. A dominance of downward propagation is confirmed by the rotary vertical wavenumber spectra of $KE_{NI}^{WKB}$ and $S_{NI}^{WKB}$ (Figure S3), evidenced by the dominant clockwise rotation of horizontal velocity and shear vectors with depth (Leaman & Sanford, 1975). Then, the vertical group speed can be estimated by identifying near-inertial wave packets and the associated downward progression of kinetic energy maxima over time (Figure 1f). We obtain a mean vertical group speed $c_{gz}^{obs}$ with one standard deviation of 61$\pm$13 m day$^{-1}$ for the six identified near-inertial events. Following Vic et al. (2021), we use mooring-based vertical group speed and vertical phase speed to constrain the vertical wavenumber $m$. For waves with frequencies close to $f$, the equation for $m$ is $(c_{\phi z}^{obs})^2 m^2 - c_{gz}^{obs} f m - f^2 = 0$, where $c_{\phi z}^{obs}$ is the vertical phase speed computed by connecting constant-phase velocity points as a function of depth. For the six near-inertial wave events, the mean vertical wavelength, $2\pi/m$, is quantified as 652$\pm$185 m.

The spatial arrangement of the mooring array also allows us to explore the meridional propagation of NIWs. Comparison of the time series of $KE_{NI}^{WKB}$ obtained from various moorings shows that the near-inertial kinetic energy peaks in the south almost always lag behind those in the north, suggesting that NIWs may propagate predominantly from north to south (i.e., equatorward in the Northern Hemisphere; Figure 2a). This indication of equatorward propagation is further confirmed by two lines of evidence. First, near-inertial kinetic energy within the mooring array is highly coherent, with the magnitude-squared coherence of near-inertial velocities $\sim$0.8 between inner moorings and $\sim$0.6 between outer moorings, consistent with all moorings having captured the same near-inertial wave events. Second, unlagged near-inertial kinetic energy peaks are commonly observed a few inertial periods before the lagged peaks (e.g., events 1,2,4,5), with the former stemming from circular inertial oscillations in the mixed layer and the latter from propagating NIWs below the mixed layer. Then, we quantify the meridional group velocity using their meridional distance and respective travel time. The travel time is identified as the temporal lag for which the lagged correlation of depth-averaged near-inertial kinetic energy in the northern and southern outer moorings is maximum. This gives a mean meridional group speed $c_{gh}^{obs}$ of 0.068$\pm$0.010 m s$^{-1}$ (5.9$\pm$0.9 km day$^{-1}$).

The frequency and horizontal scale of NIWs can be diagnosed by linking the observed group speed estimates to the dispersion relation of NIWs (see the supporting information for methodology), which is written as $(\omega^2 - f^2)m^2 = N^2k_h^2$, where $\omega$ is the frequency and $k_h$ the horizontal wavenumber. The observed $c_{gz}^{obs}$ and $c_{gh}^{obs}$ are broadly consistent with the resulting dispersion curves in Figures 2b-c. Based on these wave properties, we can obtain the mean frequency $\omega = 1.039\pm0.018f$ and the horizontal wavelength $2\pi/k_h = 79\pm28$ km from the dispersion relation. The latter is consistent with the frequency structure function diagnostics of Callies et al. (2020), who concluded that near-inertial motions have horizontal wavelengths larger than the largest scale sampled by the outer mooring array. Detailed properties of the six near-inertial events are given in Table S1.

### 3.3 Chimney effect

To assess the inertial chimney effect at different spatial scales, the vertical component of relative vorticity, $\zeta = \mathbf{k} \cdot \nabla \times \mathbf{u}$, is respectively estimated from the inner and outer mooring clusters. The chimney effect for near-inertial kinetic energy and vertical shear is illustrated by Figure 3, which displays the two-dimensional probability density functions of Rossby number, $\zeta/f$, against $KE_{NI}^{WKB}$ and $S_{NI}^{WKB}$ for all observed depths (50-520 m) and their associated vertical structures. For both spatial scales, near-inertial kinetic energy (Figures 3a-b) and vertical shear (Figures 3d-e) are found to be significantly intensified in regions of anticyclonic vorticity (i.e., $\zeta/f < 0$). Such intensification in anticyclonic regimes is more apparent for near-inertial kinetic energy, which is typically contained mostly in the first few vertical modes (e.g., Raja et al., 2022), compared to near-inertial vertical shear, which contained mostly in higher vertical modes (e.g., Alford et al., 2017). Note that the inner mooring-based Rossby number $\zeta_{Inner}/f$ reflects the signature of submesoscale flows with a positive skewness (Buckingham et al., 2016) and a range from $-0.8$ to 1.2, which is 2-3 times larger than the outer mooring-based Rossby number $\zeta_{Outer}/f$ of $-0.4$ to 0.4 (cf. Figures 3a and b). However, the enhanced near-inertial kinetic energy and vertical shear are only focused in anticyclonic regions with Rossby number values of order 0.1, rather than with those of order 1. This suggests that mesoscale anticyclones play a predominant role in determining the chimney effect.

Submesoscale processes are embedded in the field of mesoscale motions in the inner-mooring diagnostics (Figures 3a and d). To isolate the submesoscale effect, we estimate the submesoscale vorticity anomaly relative to the mesoscale background, that is, $\zeta_{Inner} - \zeta_{Outer}$. Figures 3c and f show that the association of enhanced $KE_{NI}^{WKB}$ and $S_{NI}^{WKB}$ with $(\zeta_{Inner} - \zeta_{Outer})/f$ is greatly reduced, providing further evidence that the role played by submesoscale motions is modest and thus the observed chimney effect is attributed to mesoscale motions. The detailed evolution of a near-inertial wave event with a mesoscale anticyclone environment is provided in Figures S4-5, which illustrates the sequence from the wind forc-

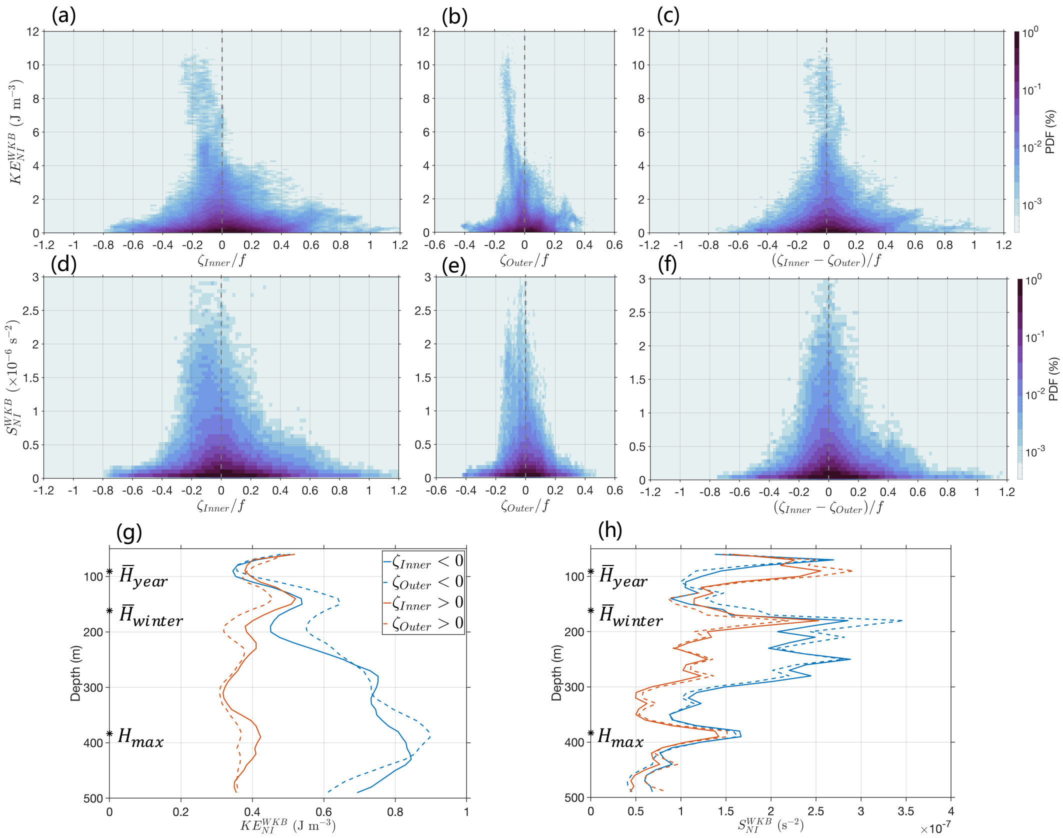


**Figure 3.** Two-dimensional probability density function of WKB-scaled near-inertial kinetic energy at the central mooring site, $KE_{NI}^{WKB}$, and Rossby number estimated from (a) the inner moorings, $\zeta_{Inner}/f$, (b) the outer moorings, $\zeta_{Outer}/f$, and (c) their difference, $(\zeta_{Inner} - \zeta_{Outer})/f$. (d-f) Same as (a-c) but for WKB-scaled near-inertial vertical shear, $S_{NI}^{WKB}$. Annual-averaged composite profiles of (g) $KE_{NI}^{WKB}$ and (h) $S_{NI}^{WKB}$ for positive and negative Rossby numbers. The annual-averaged, winter-averaged and maximum mixed layer depths are marked on the y axis of (g-h).

ing of mixed-layer inertial currents into NIWs shown as a set of discrete downward and rightward swaths below the mixed layer after approximately eight inertial periods. During the downward-propagating period, the mooring site was located inside of an anticyclonic eddy with a Rossby number of order $-0.1$, as estimated from both the outer moorings and altimetric measurements.

We next examine the vertical structures of $KE_{NI}^{WKB}$ and $S_{NI}^{WKB}$ in regions of negative and positive vorticity (Figures 3g-h). The annual-averaged mixed layer depth is about 90 m. In the mixed layer, both $KE_{NI}^{WKB}$ and $S_{NI}^{WKB}$ show no clear dependence on relative vorticity. The muted chimney effect in the mixed layer is expected because wind-forced near-inertial oscillations are purely horizontal and thus are not influenced by the sign of relative vorticity (also see Figure 4). Below the base of the mixed layer, however, $KE_{NI}^{WKB}$ associated with anticyclonic vorticity is substantially more energetic than that associated with cyclonic vorticity, typically by a factor of 2-3. This illustrates that near-inertial kinetic energy preferentially progresses downward in the presence of anticyclonic structures. In particular, the magnitude of $KE_{NI}^{WKB}$ associated with anticyclonic vorticity gradually increases with depth and peaks at 400 m, consistent with an accumulation of trapped near-inertial kinetic energy at depth.

Compared to the accumulative behavior of $KE_{NI}^{WKB}$ with depth, $S_{NI}^{WKB}$ exhibits a different vertical structure. The peaks of $S_{NI}^{WKB}$ associated with both cyclonic and anticyclonic vorticity are found around 180 m, which is very close to the mean mixed layer depth during winter (Figure 3h). Beneath 180 m, $S_{NI}^{WKB}$ associated with cyclonic vorticity rapidly decreases from $2.5\times10^{-7}$ s$^{-2}$ to about $1\times10^{-7}$ s$^{-2}$, and remains of this approximate magnitude down to 500 m. In contrast, $S_{NI}^{WKB}$ associated with anticyclonic vorticity persists with an elevated magnitude of $2.5\times10^{-7}$ s$^{-2}$ until an abrupt decrease occurs at approximately 300 m. Notably, $S_{NI}^{WKB}$ in anticyclonic regions is always larger than that in cyclonic regions from 180 m down to approximately the deepest mixed layer depth of 350 m. Below 350 m, $S_{NI}^{WKB}$, again, shows no dependence on vorticity and gently decays with depth. These results suggest that high-mode NIWs, which are expected to dominate vertical shear, are likely dissipated near the base of the mixed layer, and only low modes propagate further downward. We acknowledge, however, that accurate quantification of near-inertial kinetic energy distribution in barotropic and baroclinic modes from the moorings is particularly challenging, due to the limited sampling range (approximately one tenth of the full water column and a half of the water column above the mode-1 zero crossing; see Figure S6).

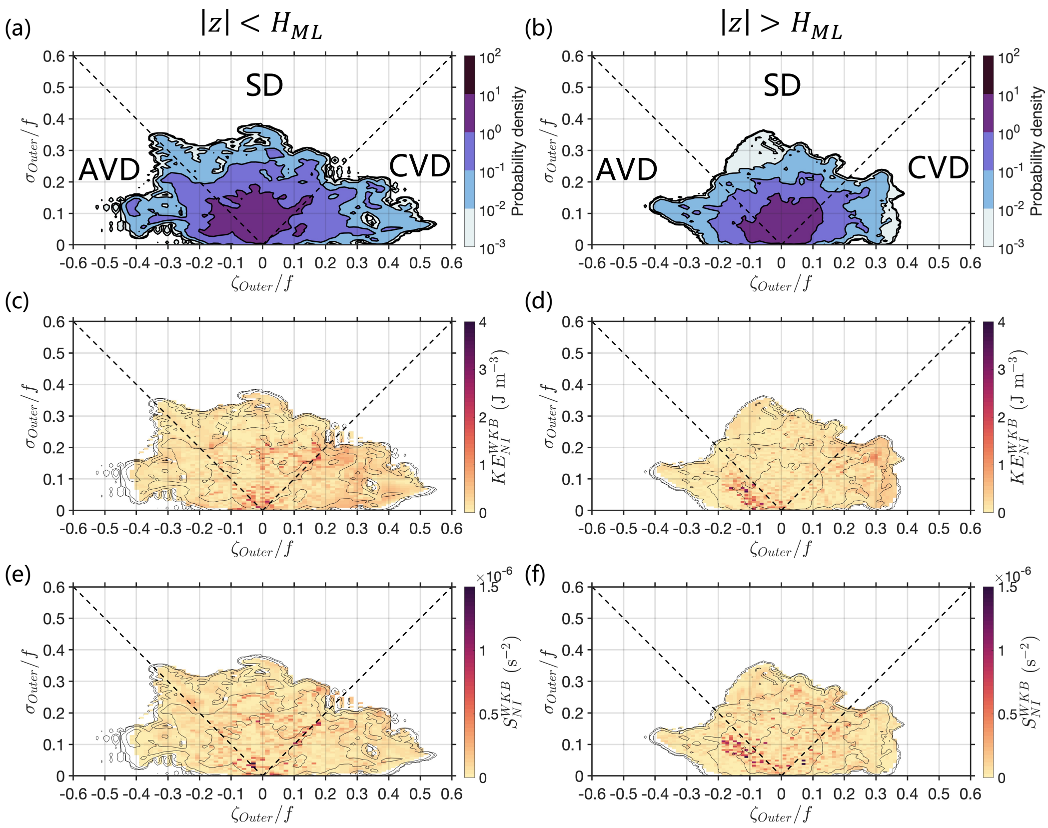


**Figure 4.** Vorticity-strain joint probability distribution function estimated from the outer moorings (a) within the mixed layer $|z| < H_{ML}$ and (b) below the mixed layer $|z| > H_{ML}$. The strain rate is defined as $\sigma = [(\frac{\partial u}{\partial x} - \frac{\partial v}{\partial y})^2 + (\frac{\partial u}{\partial y} + \frac{\partial v}{\partial x})^2]^{1/2}$. The x-y space is divided into three regions: anticyclonic vorticity dominated (AVD), cyclonic vorticity dominated (CVD), and strain dominated (SD). Conditional mean of (c-d) $KE_{NI}^{WKB}$ and (e-f) $S_{NI}^{WKB}$ conditioned on the vorticity and strain in the two vertical parts, contoured by the respective probability density.

Mesoscale straining processes may also affect the vertical propagation of NIWs by exponentially increasing the waves' horizontal wavenumbers (Bühler & McIntyre, 2005; Asselin et al., 2020; Noh & Nam, 2021). Inspired by the work of Balwada et al. (2021), we examine the distributions of $KE_{NI}^{WKB}$ and $S_{NI}^{WKB}$ conditioned on the joint probability distribution function of outer mooring-based vorticity and strain within the mixed layer ($|z| < H_{ML}$) and below the mixed layer ($|z| > H_{ML}$) (Figures 4a-b). The vorticity-strain parameter space allows us to distinguish between strain dominated regions (SD), i.e., fronts, anticyclonic vorticity dominated regions (AVD) and cyclonic vorticity dominated regions (CVD). The joint probability distribution functions below and within the mixed layer are qualitatively symmetric regarding vorticity, as expected at the mesoscales (Vic et al., 2022). Within the mixed layer, $KE_{NI}^{WKB}$ and $S_{NI}^{WKB}$ are homogeneously distributed in vorticity-strain space (Figures 4c and e). However, below the mixed layer, the largest values of $KE_{NI}^{WKB}$ and $S_{NI}^{WKB}$ are found in the AVD region (Figures 4d and f). While the straining processes may have played a role in the conversion from inertial oscillations to NIWs, the deep penetration of NIWs is found to be mostly in anticyclonic eddies rather than strained regions. A similar pattern has been found through analysis of the inner moorings (Figure S7). This confirms that mesoscale anticyclonic eddies are the primary factor facilitating the deep penetration of surface-generated NIWs. The little influence of strain on NIWs conforms to expectations from the wave escape mechanism (Rocha et al., 2018), and was also reported in a dipole vortex in the Iceland Basin (Thomas et al., 2020).

## 4 Summary and Discussion

In this work, we have examined the annual cycle of NIWs in a typical open-ocean region at midlatitudes based on mooring observations. Our main findings are summarized as follows: (1) Local wind forcing is the main factor in generating downward-propagating near-inertial motions in the OSMOSIS region. Near-inertial kinetic energy is dominated by intermittent wind events of a few days duration, and shows a seasonal cycle in energy level, elevated in winter and reduced in summer. (2) Once below the mixed layer, wind-generated NIWs are found to predominately propagate equatorward. High-mode NIWs are likely dissipated locally near the base of the mixed layer, while low-mode NIWs transfer their energy towards the ocean interior and the equator. (3) The properties of NIWs have been estimated using the dispersion relation and observations, yielding an annual-mean frequency of $1.039f$, a vertical wavelength of 652 m and a horizontal wavelength of 79 km. We also demonstrate that the meridional group speed can be predicted from the vertical group speed diagnosed from a single mooring combined with the dispersion relation. (4) The penetration of near-inertial kinetic energy and vertical shear into the ocean interior is facilitated by mesoscale anticyclones with Rossby number of O(0.1) rather than submesoscale anticyclones with Rossby number of O(1).

Our results add observational evidence for equatorward propagation of locally wind-generated NIWs, which conforms to expectations from the free propagation of NIWs due to $\beta$-refraction (Garrett, 2001). That is, waves generated at $f$, the local lowest internal wave frequency, must propagate equatorward into a latitude with an inertial frequency lower than $f$. The energy flux of these equatorward-propagating NIWs is dominated by low modes (Alford, 2003), which are associated with a faster group velocity compared to high modes and are typically expected to propagate over long distances.

The vertical structures of the chimney effect in mesoscale and submesoscale anticyclones do not show a distinct difference (Figures 3g-h), suggesting that submesoscale processes may not substantially modify the penetration of NIWs. There are three reasons for the modest effect from the submesoscale. First, submesoscale motions are typically confined to the mixed layer of O(100 m) and weaken in the ocean interior. Mixed-layer inertial oscillations may undergo lateral de-phasing caused by submesoscale motions, which would produce downward-propagating NIWs with small vertical scales, and thus the resulting vertical group velocity would be small. By contrast, mesoscale eddies are featured with a much larger vertical scale on the order of 1000 m, and thus can be a primary player in setting the inertial chimney effect at depth. Second, the spatial scale of submesoscales is comparable to the local mixed-layer Rossby radius of 1-4 km (Yu et al., 2019; Callies et al., 2020), which is considerably smaller than the diagnosed spatial scale of NIWs ($2\pi/k_h =$ 79 km). Third, both NIWs and submesoscale fronts are intermittent and short-lived in the study region, and thus the concurrence of both processes is even rarer.

Lastly, this study points out the importance of the inertial chimney effect in determining surface-generated near-inertial kinetic energy propagation into the ocean interior. However, the interactions of NIWs with eddies and associated energy transfers are not a direct consequence of the chimney effect. It has recently been suggested that the presence of NIWs can result in a substantial reduction of mesoscale kinetic energy by stimulating a forward energy cascade at partially-balanced submesoscale fronts (Barkan et al., 2021). The assessment and quantification of such cross-scale energy transfers using the OSMOSIS observations are under way.

**Acknowledgments**

We are grateful to the officers, crew, scientists and technicians of the RRS *Discovery*, RRS *James Cook*, and R/V *Celtic Explorer*, for their hard work in deploying and recovering the OSMOSIS moorings and gliders. All data are archived at the British Oceanographic Data Centre (glider data are accessible at https://doi.org/10/cqc6). This work was funded by grants from the Natural Environmental Reseatch Council (NE/I019999/1 and NE/I01993X/1). ERA-Interim data were obtained from the European Centre for Medium-Range Weather Forecasts (downloaded from http://www.ecmwf.int/en/research/climate-reanalysis/era-interim).

## References


Alford, M. H. (2003). Redistribution of energy available for ocean mixing by long-range propagation of internal waves. *Nature*, *423*(6936), 159-162.

Alford, M. H. (2020). Revisiting near-inertial wind work: Slab models, relative stress, and mixed layer deepening. *Journal of Physical Oceanography*, *50*(11), 3141–3156.

Alford, M. H., MacKinnon, J. A., Pinkel, R., & Klymak, J. M. (2017). Space–time scales of shear in the North Pacific. *Journal of Physical Oceanography*, *47*(10), 2455–2478.

Alford, M. H., MacKinnon, J. A., Simmons, H. L., & Nash, J. D. (2016). Near-inertial internal gravity waves in the ocean. *Annual Review of Marine Science*, *8*, 95-123.

Asselin, O., Thomas, L. N., Young, W. R., & Rainville, L. (2020). Refraction and straining of near-inertial waves by barotropic eddies. *Journal of Physical Oceanography*, *50*(12), 3439–3454.

Asselin, O., & Young, W. R. (2020). Penetration of wind-generated near-inertial waves into a turbulent ocean. *Journal of Physical Oceanography*, *50*(6), 1699–1716.

Balwada, D., Xiao, Q., Smith, S., Abernathey, R., & Gray, A. R. (2021). Vertical fluxes conditioned on vorticity and strain reveal submesoscale ventilation. *Journal of Physical Oceanography*, *51*(9), 2883–2901.

Barkan, R., Srinivasan, K., Yang, L., McWilliams, J. C., Gula, J., & Vic, C. (2021). Oceanic mesoscale eddy depletion catalyzed by internal waves. *Geophysical Research Letters*, *48*(18).

Buckingham, C. E., Garabato, A. C. N., Thompson, A. F., Brannigan, L., Lazar, A., Marshall, D. P., ... Belcher, S. E. (2016). Seasonality of submesoscale flows in the ocean surface boundary layer. *Geophysical Research Letters*, *43*(5), 2118-2126.

Buckingham, C. E., Lucas, N. S., Belcher, S. E., Rippeth, T. P., Grant, A. L. M., Le Sommer, J., ... Naveira Garabato, A. C. (2019). The contribution of surface and submesoscale processes to turbulence in the open ocean surface boundary layer. *Journal of Advances in Modeling Earth Systems*, *11*(12), 4066–4094.

Bühler, O., & McIntyre, M. E. (2005). Wave capture and wave–vortex duality. *Journal of Fluid Mechanics*, *534*, 67–95.

Callies, J., Barkan, R., & Naveira Garabato, A. C. (2020). Time scales of submesoscale flow inferred from a mooring array. *Journal of Physical Oceanography*, *50*(4), 1065–1086.

Chaigneau, A., Pizarro, O., & Rojas, W. (2008). Global climatology of near-inertial current characteristics from lagrangian observations. *Geophysical Research Letters*, *35*(13).

Damerell, G. M., Heywood, K. J., Thompson, A. F., Binetti, U., & Kaiser, J. (2016). The vertical structure of upper ocean variability at the porcupine abyssal plain during 2012-2013. *Journal of Geophysical Research-Oceans*, *121*(5), 3075-3089.

Dee, D. P., Uppala, S. M., Simmons, A. J., Berrisford, P., Poli, P., Kobayashi, S., ... Vitart, F. (2011). The era-interim reanalysis: configuration and performance of the data assimilation system. *Quarterly Journal of the Royal Meteorological Society*, *137*(656), 553-597.

Egbert, G. D., & Ray, R. D. (2000). Significant dissipation of tidal energy in the deep ocean inferred from satellite altimeter data. *Nature*, *405*, 775–778.

Erickson, Z. K., Thompson, A. F., Callies, J., Yu, X. L., Garabato, A. N., & Klein, P. (2020). The vertical structure of open-ocean submesoscale variability during a full seasonal cycle. *Journal of Physical Oceanography*, *50*(1), 145-160.

Ferrari, R., & Wunsch, C. (2009). Ocean circulation kinetic energy: Reservoirs, sources, and sinks. *Annual Review of Fluid Mechanics*, *41*, 253-282.

Fu, L. L. (1981). Observations and models of inertial waves in the deep ocean. *Reviews of Geophysics*, *19*(1), 141-170.

Garrett, C. (2001). What is the "near-inertial" band and why is it different from the rest of the internal wave spectrum? *Journal of Physical Oceanography*, *31*(4), 962-971.

Gill, A. E. (1984). On the behavior of internal waves in the wakes of storms. *Journal of Physical Oceanography*, *14*(7), 1129-1151.

Huang, R., Xie, X., Hu, J., & Sun, Z. (2021). Poleward propagation of typhoon-induced near-inertial waves in the northern south china sea. *Frontiers in Marine Science*, *8*, 713991.

Jeon, C., Park, J.-H., Nakamura, H., Nishina, A., Zhu, X.-H., Kim, D. G., … Hirose, N. (2019). Poleward-propagating near-inertial waves enabled by the western boundary current. *Scientific Reports*, *9*(1), 9955.

Jiang, J., Lu, Y. Y., & Perrie, W. (2005). Estimating the energy flux from the wind to ocean inertial motions: The sensitivity to surface wind fields. *Geophysical Research Letters*, *32*(15).

Kunze, E. (1985). Near-inertial wave-propagation in geostrophic shear. *Journal of Physical Oceanography*, *15*(5), 544-565.

Large, W. G., & Pond, S. (1981). Open ocean momentum flux measurements in moderate to strong winds. *Journal of Physical Oceanography*, *11*(3), 324-336.

Leaman, K. D., & Sanford, T. B. (1975). Vertical energy propagation of inertial waves - vector spectral analysis of velocity profiles. *Journal of Geophysical Research*, *80*(15), 1975-1978.

Lee, D.-K., & Niiler, P. P. (1998). The inertial chimney: The near-inertial energy drainage from the ocean surface to the deep layer. *Journal of Geophysical Research: Oceans*, *103*(C4), 7579–7591.

Naveira Garabato, A. C., Yu, X., Callies, J., Barkan, R., Polzin, K. L., Frajka-Williams, E., … Griffies, S. M. (2022). Kinetic energy transfers between mesoscale and submesoscale motions in the open ocean's upper layers. *Journal of Physical Oceanography*, *52*(1), 75–97.

Noh, S., & Nam, S. (2021). Nonseasonal variations in near-inertial kinetic energy observed far below the surface mixed layer in the southwestern east sea (Japan Sea). *Journal of Marine Science and Engineering*, *10*(1), 9.

Park, J. J., Kim, K., & King, B. A. (2005). Global statistics of inertial motions. *Geophysical Research Letters*, *32*(14).

Qu, L., Thomas, L., & Gula, J. (2021). Bottom mixing enhanced by tropical storm-generated near-inertial waves entering critical layers in the Straits of Florida. *Geophysical Research Letters*, *48*(15), e2021GL093773.

Raja, K. J., Buijsman, M. C., Shriver, J. F., Arbic, B. K., & Siyanbola, O. (2022). Near-inertial wave energetics modulated by background flows in a global model simulation. *Journal of Physical Oceanography*, *in press*. doi: 10.1175/JPO-D-21-0130.1

Rimac, A., von Storch, J. S., Eden, C., & Haak, H. (2013). The influence of high-resolution wind stress field on the power input to near-inertial motions in the ocean. *Geophysical Research Letters*, *40*(18), 4882-4886.

Rocha, C. B., Wagner, G. L., & Young, W. R. (2018). Stimulated generation: extraction of energy from balanced flow by near-inertial waves. *Journal of Fluid Mechanics*, *847*, 417-451.

Schlosser, T. L., Jones, N. L., Bluteau, C. E., Alford, M. H., Ivey, G. N., & Lucas, A. J. (2019). Generation and propagation of near-inertial waves in a baroclinic current on the Tasmanian Shelf. *Journal of Physical Oceanography*, *49*(10), 2653–2667.

Silverthorne, K. E., & Toole, J. M. (2009). Seasonal kinetic energy variability of near-inertial motions. *Journal of Physical Oceanography*, *39*(4), 1035-1049.

Thomas, L. N., Rainville, L., Asselin, O., Young, W. R., Girton, J., Whalen, C. B., … Hormann, V. (2020). Direct observations of near-inertial wave $\zeta$-refraction in a dipole vortex. *Geophysical Research Letters*, *47*(21).

Thomas, L. N., & Zhai, X. (2022). *Chapter 5 - the lifecycle of surface-generated near-inertial waves* (M. Meredith & A. Naveira Garabato, Eds.). Elsevier.

Thompson, A. F., Lazar, A., Buckingham, C., Garabato, A. C. N., Damerell, G. M., & Heywood, K. J. (2016). Open-ocean submesoscale motions: A full seasonal cycle of mixed layer instabilities from gliders. *Journal of Physical Oceanography*, *46*(4), 1285-1307.

Tort, M., & Winters, K. B. (2018). Poleward propagation of near-inertial waves induced by fluctuating winds over a baroclinically unstable zonal jet. *Journal of Fluid Mechanics*, *834*, 510–530.

Vic, C., Ferron, B., Thierry, V., Mercier, H., & Lherminier, P. (2021). Tidal and near-inertial internal waves over the Reykjanes Ridge. *Journal of Physical Oceanography*, *51*(2), 419–437.

Vic, C., Hascoët, S., Gula, J., Huck, T., & Maes, C. (2022). Oceanic mesoscale cyclones cluster surface lagrangian material. *Geophysical Research Letters*, *49*(4).

Whalen, C. B., de Lavergne, C., Naveira Garabato, A. C., Klymak, J. M., MacKinnon, J. A., & Sheen, K. L. (2020). Internal wave-driven mixing: governing processes and consequences for climate. *Nature Reviews Earth & Environment*, *1*(11), 606–621.

Yu, X., Naveira Garabato, A. C., Martin, A. P., Buckingham, C. E., Brannigan, L., & Su, Z. (2019). An annual cycle of submesoscale vertical flow and restratification in the upper ocean. *Journal of Physical Oceanography*, *49*(6), 1439–1461.

Yu, X., Naveira Garabato, A. C., Martin, A. P., & Marshall, D. P. (2021). The annual cycle of upper-ocean potential vorticity and its relationship to submesoscale instabilities. *Journal of Physical Oceanography*, *51*(2), 385–402.

Zhai, X. M., Greatbatch, R. J., & Eden, C. (2007). Spreading of near-inertial energy in a 1/12° model of the North Atlantic Ocean. *Geophysical Research Letters*, *34*(10), L10609.

Zhai, X. M., Greatbatch, R. J., Eden, C., & Hibiya, T. (2009). On the loss of wind-induced near-inertial energy to turbulent mixing in the upper ocean. *Journal of Physical Oceanography*, *39*(11), 3040–3045.

Zhai, X. M., Greatbatch, R. J., & Zhao, J. (2005). Enhanced vertical propagation of storm-induced near-inertial energy in an eddying ocean channel model. *Geophysical Research Letters*, *32*(18).